U.S. Department of Energy Collegiate Wind Competition:
Technical Design Report 2021

Written By:

Toby Barrons
Reagan Hesse
Gillian Hooper
Matthew Morganstein
Alexandra Rosenberger
John Van Dixhorn

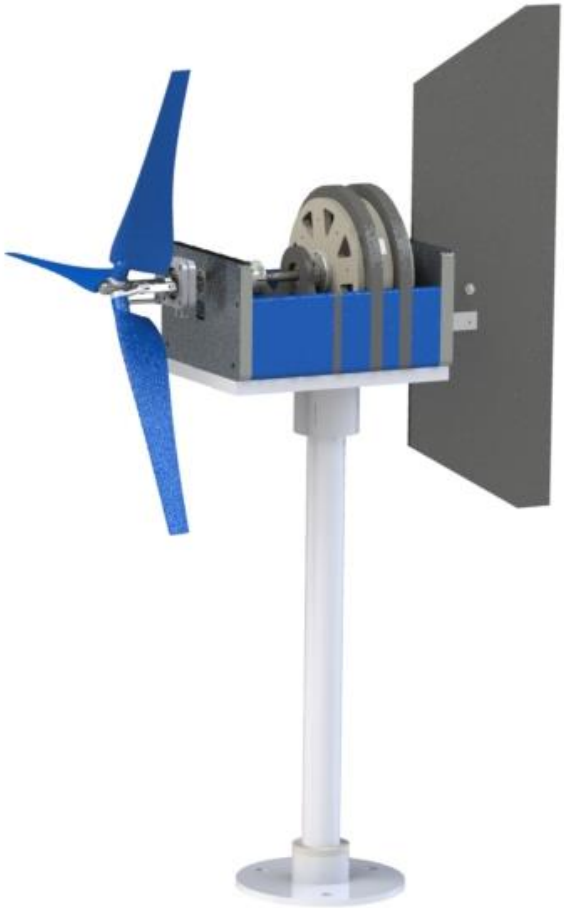

Project Advisors: Dr. Tom Nordenholz, Dr. Evan Chang-Siu, Steffan Long
CSU - Maritime Academy
23 May 2021

Table of Contents

Chapter 1: Executive Summary

The objective of this year's design was to create a fully functioning variable pitch turbine with a low cut-in speed and a completely customized generator to improve on the previous year's performance. This was accomplished through an updated variable pitch mechanism, blades, and generator construction. The final turbine consisted of 3-blades, a new variable pitch design, a passive yaw system, a custom generator, and a fixed resistive load.

The airfoils chosen for this year's turbine blade design were the SD7043 and SD7062 airfoils. Both airfoils were from the same airfoil family, resulting in similar shapes that would blend well together. The SD7043 was identified as a power generation airfoil and selected for its relatively flat slope across a C_L/C_D versus alpha graph at low Reynolds numbers. The airfoil proved its promise through testing with low start-up speeds, increased power production at higher wind speeds, and the consistency and smoothness of its power output at varying RPMs. The SD7062 airfoil was considered as a base airfoil, and primarily chosen for its thickness; this airfoil provided adequate strength at the blade's root during testing procedures.

The primary method for controlling the turbine's power output and rotor speed is the variable pitch system. Variable pitch systems allow for the use of passive control systems, which result in lower overall complexity and power consumption. The mechanism is operated by a linear actuator mounted in the nacelle, and braking is achieved by feathering the blades.

A passive yaw system was used to keep the turbine blades facing into the wind and consists of a yaw bearing assembly that allows the turbine to rotate freely about the vertical axis. A tail assembly was also created to self-align the turbine when the wind direction is changed.

A custom multi-stage, permanent magnet, axial flux generator was developed for this year's turbine. The generator was designed using a coreless stator to prevent cogging torque and lower the cut-in wind speed. The design was constructed out of Polylactic acid (PLA) using 3D-printing FDM manufacturing as the primary form of fabrication. The generator utilized modular construction techniques to allow for rapid servicing and interchanging of parts. The generator was developed to be incorporated into the final turbine structure but is also capable of operating as a stand-alone unit for sub-system testing.

The load will be set at a fixed resistance to better develop a system that generates positive power. Generating positive power at low wind speeds increases the efficiency and operating range of the turbine while also decreasing the cut-in wind speed. This simplifies the whole electrical system into two parts: the turbine-side and the load-side. The main controls associated with this system signal the actuator to some stroke length, then activate and deactivated a relay coil to switch between the fixed load and a 6V battery. This battery is also used to pitch the blades out of the braking condition, and back into the wind.

The turbine was created for multiple design conditions including performance and stress survival that were defined by wind and rotor speed. For performance, the turbine was designed to decrease startup speed, produce power up to 11m/s, and maintain that power at wind speeds above 11m/s. Factors of Safety were developed at the following four conditions: 11m/s at operating rotor speed, 18m/s at operating rotor speed, 22m/s at parked, and 22m/s at runaway.

Chapter 2: Blades

2.1 Airfoil Selection

To obtain an optimal blade geometry for the turbine, two airfoils needed to be selected based on desirable characteristics. The body of the blade consists mostly of the first airfoil, whose most desirable characteristic is power generation; this is referred to as the power airfoil. The second airfoil is placed at the root of the blade and is used to create strength; this is known as the base airfoil. To begin the selection process, airfoils were narrowed down based on the airfoil shape similarities, thickness, and smoothness, and height of the C_L/C_D versus alpha graphs. A smooth and high C_L/C_D curve indicates that the airfoil will be capable of maintaining a consistent power output over a large range of angle of attacks (AOA) which will improve the controllability of the blades. Ten base and power airfoil combinations were identified as having high-performance expectations, and from the ten blade designs, two were selected for optimization and testing. An important note is that all values were calculated at a very low Reynolds number of 50,000,

a value was chosen based on previous years' designs over the CWC operating conditions which was verified after the design process.

The first blade design selected consisted of two airfoils from the Eppler family. The power airfoil, E216, was selected due to its maximum C_L/C_D value of 40.7, and thickness of 10.4% of chord. The base airfoil, E399, is of a similar shape to the power airfoil and has a thickness of 14.8% of the chord which aids in the sturdiness of the airfoil. The airfoils comprising the second blade design are from the Selig/Donovan family. The base airfoil, SD7063, has a thickness of 14% of chord and a similar shape to the power airfoil. The power airfoil, SD7043, is thinner than the Eppler, at 9.1% of chord, which means less strength throughout the blade, but will be lighter and generate less stress on the variable pitch mechanism and is expected to increase power production. This airfoil also demonstrated a slightly lower C_L/C_D of 38.6, however, produced a smoother C_L/C_D vs AOA curve; a comparison of these two curves is shown in Figure 2.1.1. Due to the differences in C_L/C_D values, it was predicted that the Eppler blade would out-perform the SD blade during wind tunnel testing. The two blades were optimized, designed, manufactured (see Section 2.2 and 2.4), and tested (see Section 2.5). Based on these tests the SD airfoils were chosen as the final. The results in the following sections are for the SD airfoil.

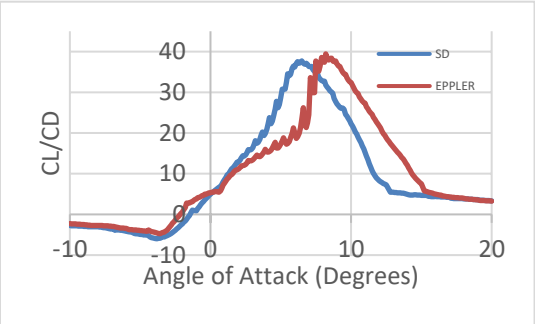

Figure 2.1.1 CL/CD Graph Comparisons

2.2 Optimization

The method used to optimize each of the blade designs was the Schmitz Optimization Method. This optimization method uses a series of equations to determine the ideal chord and twist of the blade along predetermined sections of the blade body to maximize the power captured from the wind. Each section consists of either the power airfoil, base airfoil, or a mixture between the two, with the base airfoil focused towards the bottom of the blade body and the power airfoil concentrated towards the tip. During the initial optimization stages, 10 sections were created along the body of the blade, with the far bottom section being composed of the base airfoil, one blended section consisting of 50% base and 50% power above the base airfoil section, and the remaining 8 sections being composed of the power airfoil.

This division of the blades' composition was done through Qblade, an open-source program that uses BEM Theory and XFOIL to analyze and generate graphs comparing important blade characteristics. The graphs produced for the airfoil analysis provided comparisons of the coefficient of lift (C_L) versus angle of attack (α), which are two variables used in the Schmitz optimization equations.

2.3 Analysis

2.3.1 Performance

Qblade was also used during the analysis process to find theoretical performance curves. An important analysis conducted was that of the full blade and rotor designs, which utilized the BEM analysis aspect of Qblade. This included a graph of coefficient of power (C_P) vs tip speed ratio (TSR), at different pitch angles for the SD blade, seen in Figure 2.3.1. Each line represents a different pitch angle varying from zero to negative thirty in five-degree increments, a negative pitch represents the leading edge towards the wind direction, known as feathering. These graphs were used

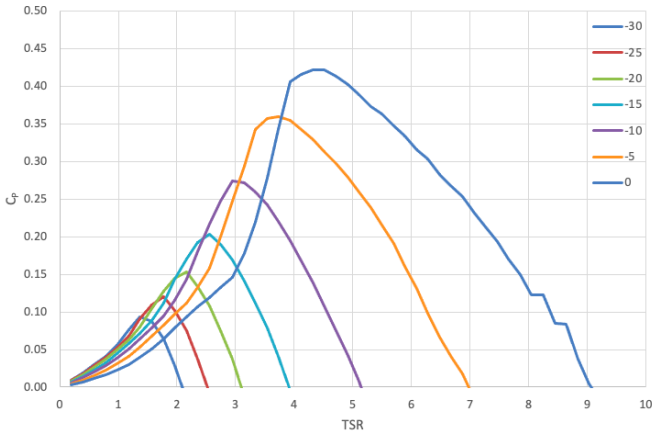

Figure 2.3.1 C_P vs. TSR

to determine the expected power extraction at different wind speeds and pitch angles. These curves needed to be high and flat for best performance and controllability.

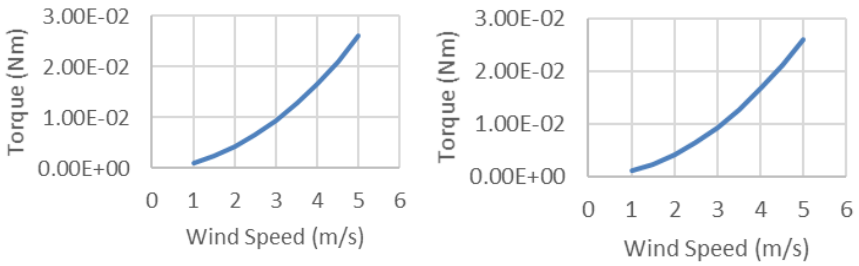

Figure 2.3.2 Startup Speed

This analysis also provided a torque versus wind speed graph, which proved useful for determining a theoretical startup value. The torque that the blades came overcome with a rotor speed of zero RPM at specific wind speeds for the SD blade is shown in Figure 2.3.2. Finding the torque that is expected to be created by the generator and finding at what wind speed the blades are capable of overcoming that torque provides an estimate for the startup speed. In addition to these graphs, a Reynolds number versus radial position graph, shown in Figure 2.3.3, was also generated and used to verify that the turbine was running at a Reynolds number of 50,000 at a wind speed of 11m/s and operating rotor speed.

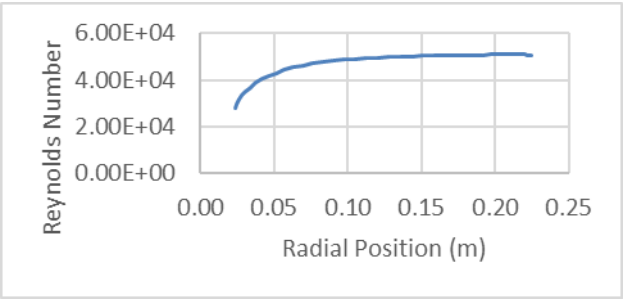

Figure 2.3.3 Reynolds Number

These graphs and analyses helped to determine theoretical performance and narrowed down blade designs. However, these analyses are not completely accurate due to inaccuracies in the aerodynamic modeling as well as additional losses in the system, which meant all final decisions were based on testing data.

2.3.2 Stress

The stress calculation was meant to predict the amount of stress and deflection the blades would endure during different wind and operating conditions. These calculations were found at 11m/s, 18m/s, and 22m/s winds, where the blade was treated as a cantilever beam fixed at the root. For each of the 40 blade sections at their given r, the axial force (F) across each section could be determined by multiplying the mass of the blade from the section at r to the tip and its centripetal acceleration (A_r) ($F = mA_r$). The mass of each section was obtained using a trapezoidal integration method, with the total blade from base to tip is 0.018 kg. The centripetal acceleration was approximated using the following equation (Equation 2.3.1):

$$A_r = \frac{(R + r)\omega^2}{2}$$

Equation 2.3.1

This equation is represented by R the outer radius of 0.225, r the radius of each section along the blade body, and ω the speed of the blades in radians/s. From here the stress at each blade section could be found by dividing the axial force (F) by the r of each section, which is the stress due to centrifugal loading represented by sF.

To determine the total flapwise deflection and the max stress of the blade under these wind conditions, the shear and bending moment needed to be calculated along each of the 40 sections. The shear could be found by integrating the flapwise aerodynamic loading, F_n, found in Qblade across each r to the outer radius R. The bending moment is found by integrating the shear in the same manner. The max stress, sM, could then be calculated with the Flexure formula, evaluated at the surface of the blade. An approximation was used for the area properties in the airfoil [12]. The max stress at each blade r cross-section, $sTotal$, could then be found by adding the sF and sM together. The stress distribution across the body of the blade at 11m/s winds can be seen in Figure 2.3.4, with the highest stress values occurring between 0.1 m and 0.15 m along the blade.

When determining deflection, the curvature and slope of the blade were each integrated to find the final deflection, v, value of each section. The curvature can be found by dividing the bending moment by the modulus of elasticity and the area moment of inertia. Once the curvature was calculated, this value was integrated across each r starting at the hub to the outer radius R to find the slope of the curve. Using the slope, v', the deflection could be calculated through integration. A max deflection of 0.001982 m was found at 11m/s winds.

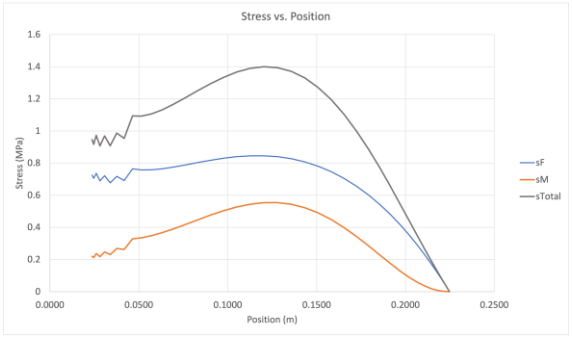

Figure 2.3.2 Stress vs. Radial Position

The root designed for the blade was a female type root, seen in Figure 2.3.5, and the pullout stress was calculated to determine the axial and shear stress at the set screw connecting the blade to the blade mount. For each of the conditions considered, the axial force (F_o) at the root was evaluated using the previous analysis. The maximum allowed stress of the PLA material was determined to be around 41 MPa, based on a series of previously conducted experiments in the Cal Maritime lab, and observed to have little to no plastic deformation before ultimate failure. The root stress and ultimate stress of PLA were used to determine a factor of safety for each condition which is seen in Table 6.1.1.

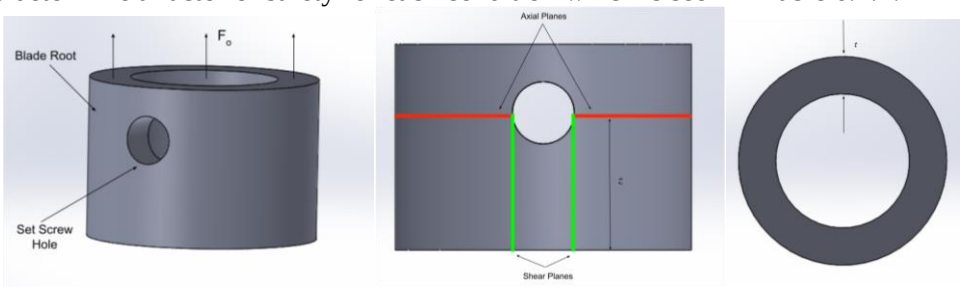

Figure 2.3.5 Female Root Assembly

The axial stress on the root based on these parameters was found to be about 49 MPa and was calculated using the equation below (Equation 2.3.2). This value is higher than the maximum allowed force, presenting with a safety factor of 0.84. The shear stress was calculated using the equation below (Equation 2.3.3), where z is the distance from the base of the root to the center of the screw, t is the thickness of the blade from the inner diameter to the outer diameter and K is the stress concertation factor [13].

$$\sigma = \frac{KF_o}{A}$$

Equation 2.3.2

$$\tau = \frac{F_o}{4zt}$$

Equation 2.3.3

2.4 Manufacturing

The airfoil and Schmitz optimization values were brought into Qblade to create the blade model. This model did not include an attachment root for the hub which required a root design to be created and attached in Solidworks. The blade design and created root were attached and made into an assembly and exported as an STL. The blade was then 3D printed on an Ender 5-plus using Polylactic Acid (PLA) and an infill of 100%.

2.5 Testing

2.5.1 Initial Screening

To determine the best blade design from the Eppler and Selig/Donovan combinations, both designs were tested in the wind tunnel against a control blade. The control blade and generator that was used for this test came from previous Cal Maritime CWC Teams: the control blades were developed by the 2018 Team, which were a combination of Gottingen 195 and 430 airfoils, and the control generator was from the 2020 Team. For an even comparison, both blades were designed to the same TSR (λ) value.

The first test performed for both blade designs was a startup speed comparison. During this comparison test, the blades were placed under no load, while the wind speed was slowly increased until the blades began to spin. This wind speed was measured using a LabVIEW DAQ set up and documented as the Startup speed; the rpm of the blades was also measured and documented at this time. It was determined from this test that the SD blade design had the lowest startup speed, see Table 2.5.1.

The second test performed on the three sets of blades was a power analysis test. This test began with setting the wind tunnel at a predetermined wind speed of 5m/s, 8m/s, and 10m/s, and applying a load on the generator that was varied between 10 and 100 ohms at intervals of 10. At each load, the turbine RPM, voltage, and current were measured and documented; the RPM was measured using an RPM gun, and the voltage and current were found using the LabVIEW display. The voltage and current values were then used to confirm the set resistances and calculate the power output of the turbine at each resistance value. The max power was identified for each wind speed, and graphs of the power output vs. rpm, as well as the expected max power at 11m/s, were created for further analysis; the prediction values were calculated using the equation below, Equation 2.5.1, which is a rough approximation that assumes the coefficient of power is the same at both wind speeds, where $MP_{@\,10}$ represents the max power at 10m/s.

$$MP_{@\,11} = MP_{@\,10} \times 1.1^3$$

Equation 2.5.1

Figure 2.5.1 displays the produced power curves at 10m/s wind speeds, and Table 2.5.1 displays the max power of each blade at the three tested wind speeds. The powers are highlighted from highest to lowest produced power in green, yellow, and red. From these graphs, it was concluded that at every wind speed one of the blades was producing more power than the control blade. This test determined that the Eppler and SD were producing close to the same amount of power with the SD starting out producing less power, but then inching ahead as the wind speeds increase. The generated curves show that at each wind speed all the graphs are falling on similarly flat curve shapes.

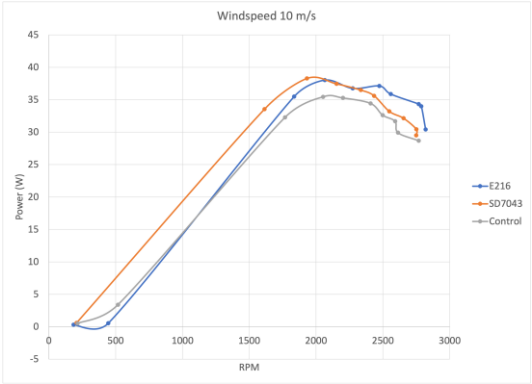

Figure 2.5.1 Testing Power Curves at 10m/s

Blade	Startup Speed	Power @ 5 m/s	Power @ 8 m/s	Power @ 10 m/s	Expected Power @ 11 m/s
Control	4.0 m/s	3.6 W	14.6 W	35.5 W	47.2 W
SD	2.8 m/s	3.3 W	15.9 W	38.3 W	51.0 W
Eppler	3.6 m/s	3.7 W	16.6 W	38.0 W	50.6 W

Table 2.5.1 Test Results

2.5.2 Blade Optimization

Once the airfoils were selected, the rest of the semester was spent changing different aspects of the optimization equations to find the optimal design. To begin the blade was printed with a TSR of 4.5 which created a much thinner blade and was expected to generate more power. The TSR is the main input for the optimization and the higher the value the smaller the chord, according to the Schmitz optimization. However, once placed on this year's turbine it was discovered that by using a larger TSR the blades performed poorly on startup. This led to printing the blades at a TSR of 4 which was expected to have a better startup speed, but also decrease the power production. This required testing to determine if the decrease in startup speed would be worth the power loss. In the end, the TSR of 4 cut the startup speed by about 3m/s and decreased the power only slightly. This resulted in the final design being optimized with a TSR of 4.

2.6 Final Design

The final airfoils selected were the SD7043 and SD7062 with three interpolated combination blades that were 25% SD7043 with 75% SD7062, a direct 50/50 split, and a 75% SD7043 with 25% SD7062 mix. The airfoil consisted of 41 sections with the base and intermediate blades accounting for the first eight, the rest were the power airfoil. The TSR selected was 4 which provided a compromise between an effective power production as well as low start-up speed. This blade was capable of withstanding all expected operating conditions but would break if the rotational speed reached above 7700 RPM. If this condition became necessary, the material of the blade could be changed to withstand the force. An 11-section summary of the final blade geometry can be seen in Table 2.6.1.

Section	Radius (m)	Chord (m)	Twist (º)	Airfoil
1	0.0234	0.052	39.22	SD7062
2	0.0435	0.059	29.10	25/75
3	0.0637	0.055	21.89	50/50
4	0.0838	0.049	16.82	75/25
5	0.1040	0.043	13.19	SD7043
6	0.1242	0.038	10.50	SD7043
7	0.1443	0.034	8.44	SD7043
8	0.1645	0.030	6.83	SD7043
9	0.1847	0.027	5.54	SD7043
10	0.2048	0.025	4.49	SD7043
11	0.2250	0.023	3.61	SD7043

Table 2.6.1 Final Blade Geometry

Chapter 3: Mechanical

3.1 Overview

The mechanical components of the wind turbine include the tower, tail, nacelle, and variable-pitch assembly. The majority of the mechanical components are made out of 6061 aluminum. However, the tail was plasma cut from a 1/16" steel sheet. The rest of the components were manufactured using a combination of manual mill and lathe along with a Hass CNC mill. These components, along with fasteners and bearings obtained from McMaster-Carr, make up the mechanical assembly of the turbine.

3.2 Variable Pitch

The variable pitch assembly is made up of five main components: the main hub, three blade mounts, three pitch levers, the pitch driver, and the actuator connection clip. The blade mount is secured to the base hub with a shoulder screw which is separated from the blade mount by a PTFE bushing to prevent friction. The blade mount and pitch driver are connected by the pitch levers, which are attached with ultra-low-profile shoulder screws. The pitch driver is the piece moving axially along the base hub, pushing all three pitch levers and in turn rotating all three blade mounts simultaneously. The actuator connection clip is the only piece in this assembly that is not spinning with the turbine and is connected to the pitch driver with a 5/8" shaft ball bearing. The inside of the ball bearing spins with the pitch driver while the outside stays stationary and connects to the actuator connection clip. Figure 3.2.1 shows this assembly with the labeled components.

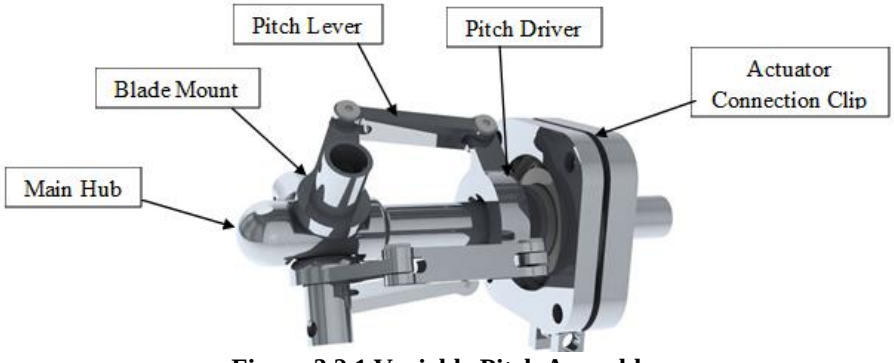

Figure 3.2.1 Variable Pitch Assembly

3.2.1 Finite Element Analysis

To ensure the variable pitch mechanism would not fail due to stresses in the system, finite element analysis was performed on all parts with failure potential. Analysis was done at the turbines rated speed of 2420rpm as well as the extreme condition of 8500rpm. The results of the analysis are shown in the far-right column of Table 6.1.1.

The weakest component in the variable pitch system is the blade mount screw, which holds the blade mounts to the main hub. They experience the same force as the blade stress force which is described in Section 2.3.2. The analysis at the extreme condition is shown in Figure 3.2.2. The fixed geometry was the upper end of the threads as that area is what holds the screw from coming out of the hole while under centripetal force. The force is on the bottom of the head because that is what makes contact with the blade mount. Through this analysis, the factor of safety at the rated speed is 1.24 and the factor of safety at the extreme condition is 0.15. This means under all operating conditions, the turbine will not fail but if the turbine fails to pitch at a high wind speed, the whole mechanism will fail.

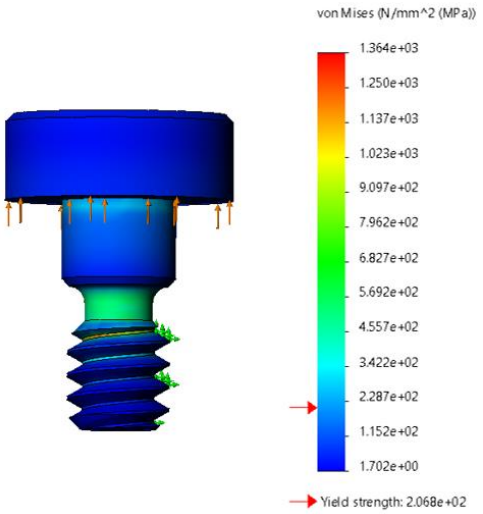

Figure 3.2.2 Blade Mount Screw FEA

3.3 Actuator

For the variable pitch system to work, a linear actuator is needed to control the angle of the blades. Choosing the wrong actuator would be devastating to the system, therefore determining the correct actuator size was a necessity. Rotational speed, wind speed, air density, blade geometry, blade angle, and the geometry of the variable pitch mechanism are all factors that contribute to calculating the force necessary to change the angle of the blades. The necessary actuator force (Equation 3.3.1) can be derived as a function of angle by using the free body diagram shown in Figure 3.3.1.

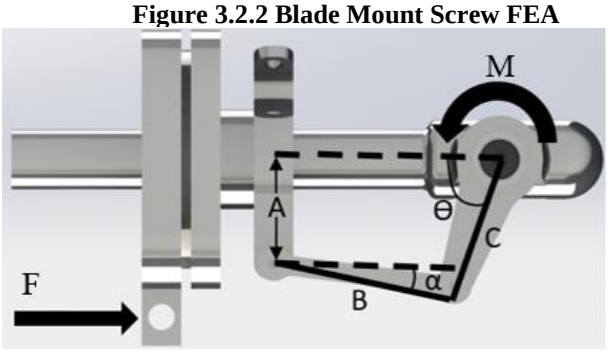

Figure 3.3.1 Variable Pitch Geometry

$$F = \frac{3M\cos(\alpha)}{C\sin(\alpha+\theta)}$$

Equation 3.3.1

$$M = \frac{1}{2}C_m\rho_{air}\int_0^R \sqrt{U_{wind}^2 + (r\Omega)^2}\, c^2 dr$$

Equation 3.3.2

The pitch moment created by the blades is found using Equation 3.3.2. The moment coefficient (C_m) used was the largest value found over the full range of attack angles through the Qblade program. Only the largest value was used to represent a worst-case scenario. The integral is run from the base of the blade to the max length (R) where r is the length along the blade. The chord length (c) of the airfoil changes along the length of the blade; the values of this are shown in Table 2.6.1. Wind speed was set to 18m/s and rotational velocity (Ω) was set to 2420rpm which represents the highest force the turbine will face while operating. The air density used was $1.143*10^{-7}$ blobs/in^3. Using Figure 3.3.1, the force required for the actuator was found to be 1.35lbf or 6N. The results of the analysis are shown in Figure 3.3.2.

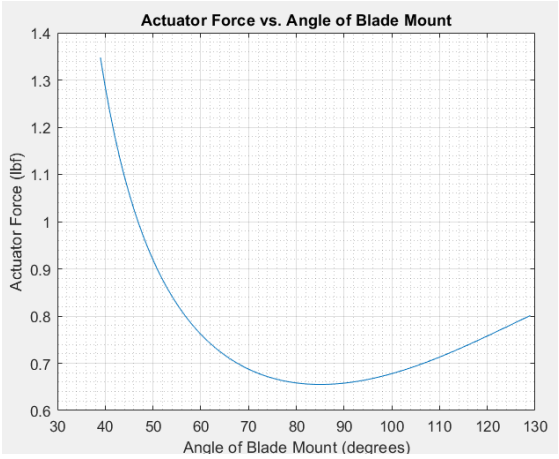

Figure 3.3.2 Actuator Force vs. Angle of Blade

The actuator also had to cover a range of angles from 39º to 129º. Referencing Figure 3.3.1, the required stroke length of the actuator can be derived as a function of angle. Using Equation 3.3.3 the stroke must be at least 1.2 inches or 31mm. The length of the actuator stroke compared to the angle of the blade mounts can be seen in Table 5.3.1.

$$L = [B\cos(\alpha_2) + C\cos(\theta_2)] - [B\cos(\alpha_1) + C\cos(\theta_1)]$$

Equation 3.3.3

With advice from the 2020 Cal Maritime CWC team, Actuonix Motion Devices was the company used to select the actuator. Based on the force and length found in the calculations, a L12-I was selected with the highest gear ratio available at 210:1 and a stroke length of 50mm. The high gear ratio gives a maximum driving force of 80N and a maximum back drive force of 45N.

3.4 Nacelle

In this design, seen in Figure 3.4.1, the purpose of the nacelle is to mount the generator, attach the tail, attach the actuator, and support the weight of the turbine assembly. The two end caps that make up the nacelle were made of 6061 Aluminum and were machined to provide an accurate alignment of the main drive shaft by press-fitting bearings in both. For the front-end cap, there is a hole placed in the plate to allow the actuator rod to connect to the variable pitch assembly. The piece behind the front-end cap is considered the actuator mount. This is made of PLA and has four holes to screw down the actuator, and two bigger holes to mount the whole assembly to the nacelle bottom plate. For the rear-end cap, there are four threaded holes (8-36) to mount the L-brackets of the tail assembly along with the bearing holes. In each of the end caps, there are four clearance holes to fit the four threaded rods that are used for the generator. The bottom nacelle plate is made to attach the whole upper assembly by use of four threaded holes (1/4”-20). The bottom plate also has four counterbored clearance holes that house 5/16”-24 screws which thread into the yaw bearing housing, connecting the turbine to the tower. There is a 0.5” hole to run wires down from the turbine down the tower and to the electrical system.

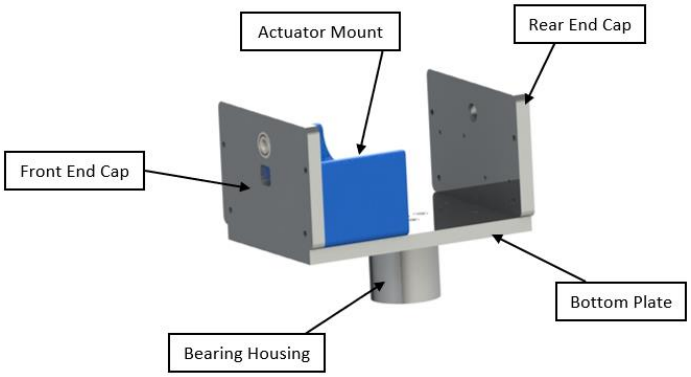

Figure 3.4.1 Nacelle

3.5 Passive Yaw

A passive yaw system will be used to ensure the turbine’s blades are always into the wind to perform at the highest efficiency. The passive yaw system consists of two parts: the tower assembly and the tail assembly. The tower assembly, shown in Figure 3.5.1, is influenced by the 2019 Cal Maritime CWC team’s design. The 3/4” shaft-diameter ball bearing is press-fit into the bearing housing. The bearing housing attaches to the bottom plate of the nacelle with four 5/16”-24 screws. The bearing is then attached to the tower by being press fit around the tower connection which is held in the tower using 8-32 set screws. This assembly allows the whole turbine to rotate freely about the vertical axis. The tail was plasma cut from a sheet of 1/16” steel. It is attached to the rear end cap by two L brackets, both with two 8-36 screws and nuts. The tail assembly is shown in Figure 3.5.2.

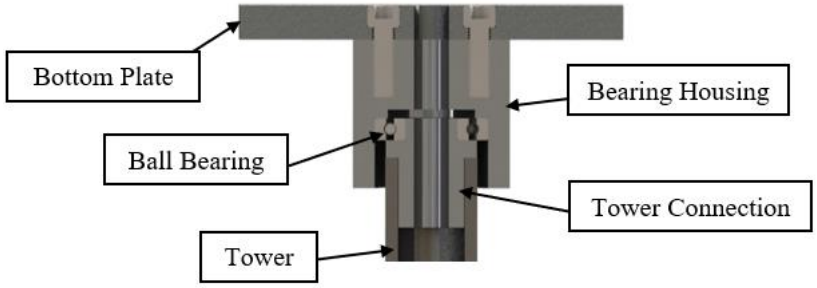

Figure 3.5.1 Yaw Assembly

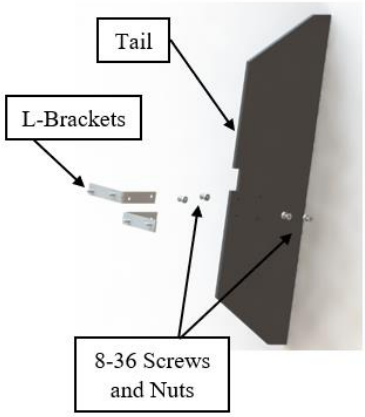

Figure 3.5.2 Tail Assembly

When the incoming wind direction is changed, the tail is no longer parallel to the wind. This creates an aerodynamic moment that realigns the tail with the wind and therefore the whole turbine. The whole tower assembly from the base plate to the tower connection is

held together by set screws. This was done so the turbine could have an adjustable height. The Cal Maritime wind tunnel is smaller than the competition wind tunnel, so adjustability was necessary. To change the height of the turbine, all that is needed is a new tower shaft at a different length, with set screw holes.

Chapter 4: Generator

4.1 Overview

The 2020 Cal Maritime CWC team chose to design and manufacture a custom generator based on the previous experiences of Cal Maritime teams, and observations of the downfalls of commercially available motors for competition tasks. Commercially available motors are optimized for constant operation at high speed and often do not contain mitigations for cogging torque or provide means for refining the power curve of the turbine. Cogging is a resistive torque generated from the interaction between ferrous metal and a magnetic field. Cogging along with frictional resistance and rotational inertia must be overcome before a generator can begin producing positive power. To perform well in the cut-in wind speed task, cogging torque must be minimized. For this reason, the decision was made to develop a custom coreless generator, in which no ferrous material was to be utilized in the construction of the machine's stator.

The 2020 Cal Maritime CWC team chose to develop a coreless radial flux machine. The final generator design performed well in initial testing and proved to be a superior alternative to previous years' purchased generators with a decreased cut-in speed power and comparable power generation at rated wind speeds. Radial flux machines are an attractive choice for CWC due to their manufacturing simplicity as well as competition-size constraints and aerodynamic factors which limit the overall size of the turbine generator to approximately 5" in length by 6" in diameter. With a limited volume, a single stator and single rotor radial flux machine can hold significantly more windings, at a thicker gauge, and over a larger area than an equivalent axial flux machine, making the radial flux a superior choice for the given configuration. This discrepancy between the two topologies can be overcome by breaking an axial flux machine into multiple stages of stators and rotors. Coreless radial flux machines are not without downsides. Lacking ferrous material in the stator winding and with only poles on the one side of the stator, coreless radial flux machines have inefficient magnetic flux circuits. This problem can be addressed in part through the use of a Halbach array magnet arrangement which improves magnetic flux projection leading to a more complete magnetic circuit through the coils and higher flux density across the air gap. A Halbach array was employed by the 2020 generator design team to great effect.

With the success of the 2020 generator design, it would have been reasonable to equip the 2021 turbine with an exact reproduction of the 2020 generator design less some marginal improvements such as the use of square wire windings, a slight reduction in the number of coil windings, and a slight reduction overall generator size. However, due to surplus team capacity, the decision was made that an entirely new design should be attempted to provide the best learning outcomes, improve design efficiency, and furnish future Cal Maritime CWC teams with additional data on generator design. For these reasons, a two-stator, three-rotor coreless axial flux machine was developed. While unique in its design, the new generator leveraged lessons learned from 2020 and was developed using similar manufacturing techniques such as FDM 3D printing and modular construction for rapid prototyping.

4.2 Axial Flux

4.2.1 Theory

All permanent magnet generator designs rely on the same basic principles of electromagnetic induction. Faraday's law of induction states that a time-varying magnetic field through a loop of conductor will cause a voltage to be "induced" in that conductor. In a permanent magnet generator, the

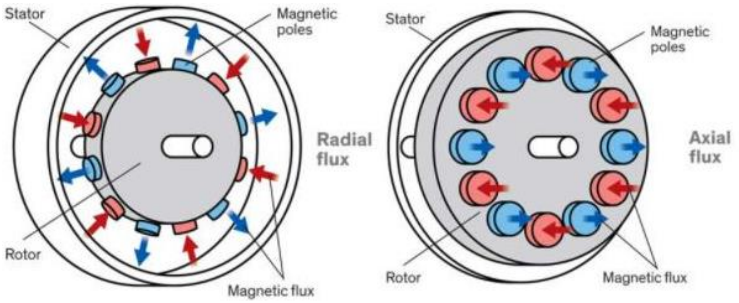

Figure 4.2.1 Magnetic Flux Topology Diagram [7]

changing magnetic field is generated by moving alternating polarity magnets in relation to the coil windings. The first step in permanent magnet generator design is the selection of the magnetic flux topology. In radial flux machines, the magnetic flux is aligned radially and produces flux that is perpendicular to the axis of rotation. In axial flux machines, the coil and magnets are arranged such that the magnetic flux is aligned axially along the length of the machine. A depiction of the two magnetic topologies is shown in Figure 4.2.1.

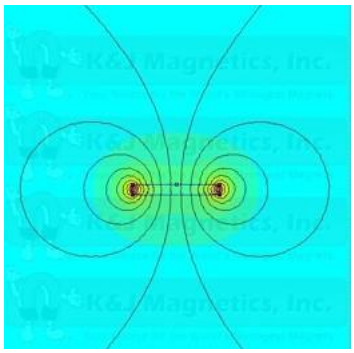

In selecting a flux topology, it is important to recognize that magnetic flux emittance is not uniform across the surface of a magnet. Magnetic flux attempts to travel in closed loops between the opposite poles of a permanent magnet creating parabolic flux lines from one pole to another. An example of how magnetic flux emanates from a permanent magnet is pictured in Figure 4.2.2 on the right. Normally, the iron or ferrous metalcore in the stator of a radial generator helps direct the magnetic flux through the conductor loops. Without a ferrous core, many of the strongest flux lines do not pass directly through the coil windings and their potential voltage induction is lost. This problem can be addressed in axial flux generators through the use of multiple rotors. With multiple rotors, opposite magnetic poles can be placed on either side of the conductor loops in the stator. These opposite poles align the magnetic field lines perpendicular to the conductor loops and create a complete magnetic circuit through the generator. This effect is depicted in Figure 4.2.3 and was a primary factor in the selection of an axial flux topology for the generator design.

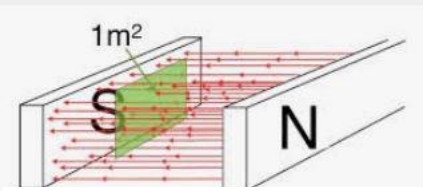

When theoretically evaluating a generator design the voltage constant is the primary performance characteristic of concern. The voltage constant is a measure of the voltage produced in a generator divided by its rotational speed. This value can be used to predict the voltage produced by the generator at any operating speed. Furthermore, if the load on the generator is known along with the internal winding resistance, the power produced by the generator can also be determined. The following equation was used to estimate potential generator designs characteristic DC voltage constant to determine their viability for use in the competition. This equation was derived from Faraday's law with corrections for rectifying from AC to DC.

$$\frac{V_{DC}}{n} = \frac{\sqrt{3}}{20} N B_{max} A p q k_w$$

Equation 4.2.1

In Equation 4.2.1, N is the number of turns per coil, B_{max} is the flux density at the face of a magnet, A is the area of a coil, p is the number of magnet poles in a rotor, q is the number of coils per phase, and k_w is the winding factor. The goal of the final generator design was to maximize the terms on the right-hand side of the equation within their design limits to produce the optimal voltage constant for the competition tasks and the 48V output limit.

4.2.2 Design

A two-stator, three-rotor configuration was selected for the generator. Due to the 6in diameter size constraint, it was determined that a single stator would not be capable of producing sufficient power as the total area of the coils and the number of windings would be too restricted, hence a two stator design was selected. The two stator configuration allowed for twice the coil area and double the number of

windings to be used within the 6in diameter size limit. Three rotors were included in the design to take advantage of the aforementioned magnetic flux alignment advantages for each stator. The number of poles and coils was determined based on the geometry of the stator, winding factor, and considerations of manufacturing complexity. Using a winding factor calculator, the optimal coil/pole number was determined to be 9 coils per stator with 8 poles per rotor. This solution yielded the largest winding factor while maintaining manufacturability. The exact winding scheme for the first stator is shown in Figure 4.2.4.

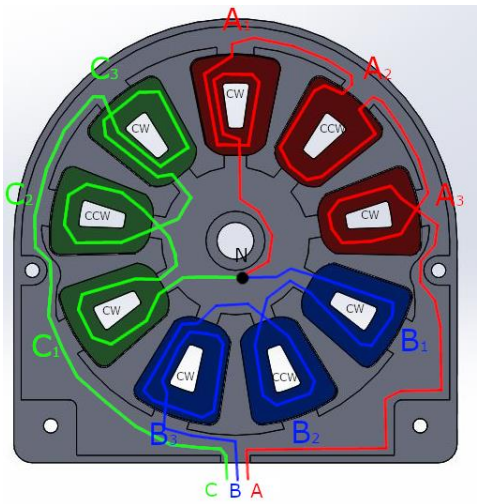

Figure 4.2.4 Stator 1 Winding & Wiring Scheme

Each stator was designed to contain three coils per phase. Each respective coil was wired in series in clockwise-counterclockwise-clockwise configurations. Each stator was wired in a wye configuration with the neutral lines connected in stator one. The two stators were wired together in series such that the outputs of each phase in stator one became the inputs for stator two. Other wiring configurations such as Delta-Delta, Wye-Delta, and a parallel-connected Wye-Wye design were testing during initial prototyping. The Wye-Wye series configuration was selected because it offered the highest efficiency while ensuring that the current in two stators remained equal during operation. Equal current in each stator is advantageous because it allows for a consistent wire gauge to be used throughout the generator. If one stator was to carry more current than the other, different considerations for heat dissipations and copper losses would have to be made for each stator, complicating the overall design. 20 AWG enameled copper wire was chosen for the generator designs based on its current threshold and heat dissipation under load. Testing conducted by the 2020 team confirmed that 20 AWG can comfortably carry 2 amps for 30 minutes without heating enough to compromise the PLA used the stator and coil structures. Additional testing was carried out this year at 2.5 amps for 5 minutes which further confirmed the selection of 20 AWG. The final wiring schematic for the two stators is shown in Figure 4.2.5.

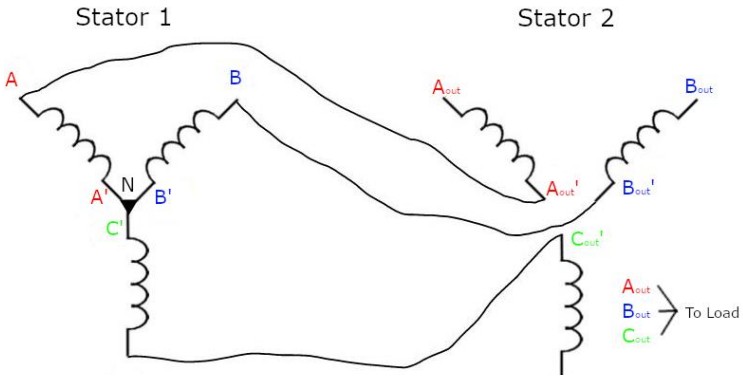

Figure 4.2.5 Wye to Wye Series Stator Connection

The coils were designed with a trapezoidal geometry to maximize the coil area for the given stator geometry. In their current configuration, the area of each of the coils is approximately 1.79in^2 for a total coil area of 16.11in^2 per stator. The total effective area for coils on each stator is approximately 19.63in^2 which means that 82% of the effective stator area was utilized for windings. Efficient use of stator space allows for the greatest coil area for a given stator size which improves a generator's output per unit of volume, something which is critical given the competition's size constraints. Each coil was wound with 40 turns of wire for a total of 240 turns per phase. The rotors each utilize eight N52 1”x1/2”x3/16” neodymium magnets which produce 3,237 peak Gauss (at each magnet surface). The generator incorporated a modular design to allow for servicing and

Figure 4.2.6 Final Generator Exploded View

interchanging of individual parts in the case of failure or part testing. Parts were designed to minimize the use of adhesives and complex fasteners. The outer rotor can be quickly detached with two screws. The stators feature a clamshell design so they can be easily opened to inspect wiring or exchange coils. The final generator was incorporated into the overall turbine structure, but modular structure pieces were developed so the generator can be tested as a standalone unit apart from the main turbine. The modular design allowed for generator parts to be printed on a large variety of 3D printers as no single part dimension exceeded standard print volume limits. Figure 4.2.6 showcases the various modularity of the generator assembly.

4.3 Component Testing

4.3.1 Magnets

Of the litany of variables that determine voltage constant in Equation 4.2.1, the magnetic flux (B_{max}) term is typically the most difficult to accurately predict. The use of multiple rotors in a multi-stage axial flux machine further complicates the task of accurately predicting B_{max} in the theoretical design stage. The 2020 CWC generator design team noted a significant discrepancy of 150% between their theoretical voltage constant and their experimentally measured voltage constant in their final design. It was theorized that this discrepancy was largely attributed to the uncertainty of the B_{max} term during their initial design phase. To mitigate this error and in pursuit of a more accurate theoretical prediction, electromagnetic modeling software (EMS) was utilized along with extensive gauss meter testing during the design and prototyping phase this year. EMS tools were used to model magnetic flux variance axially along the generator to determine the average magnetic flux through the coil windings. Figure 4.3.1 shows this process for the prototype design.

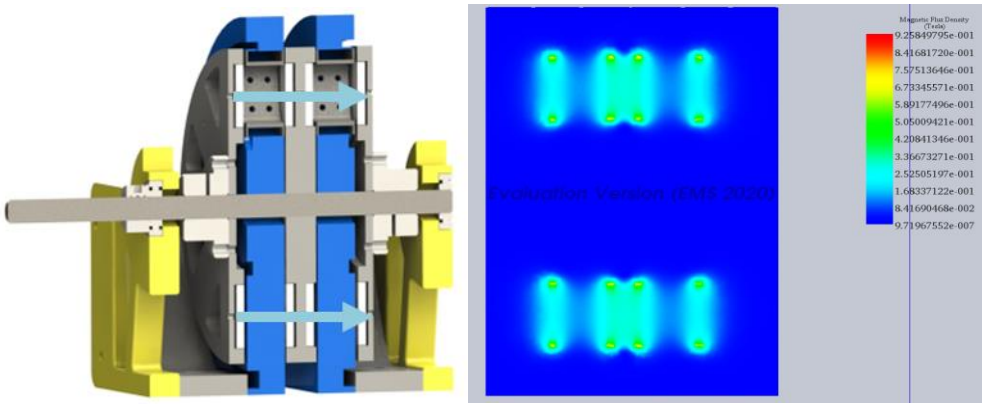

Figure 4.3.1 Electromagnetic Flux Modeling Using EMS

Additional gauss meter experimental data was gathered to better understand how magnetic flux varied across the face of the permanent magnets. A magnet test stand was developed with the gaussmeter probe located in the locked spindle of a vertical axis mill. The mill table was then moved at defined increments and magnet flux readings were recorded across the face of the magnet. An example of the test setup is shown in Figure 4.3.2 on the right. The result of the measurements is shown in Figure 4.3.3 below. Measurements were taken in the top left quadrant of the magnet as it was assumed that the flux profile was symmetrical across the vertical and horizontal axes of the magnet surface.

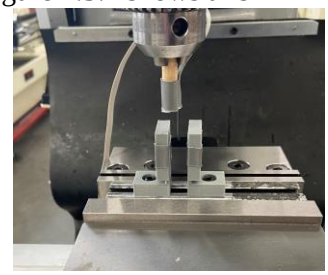

Figure 4.3.2 Magnet Testing

0.25	0.24	0.23	0.23	0.22	0.21	0.2	0.2	0.19	0.18	0.17	0.16	0.16	0.15	0.14	0.13	0.13	0.12	0.11	0.1	0.09	0.09	0.08	0.07	0.06	0.05	0.05	0.04	0.03	0.02	0.02	0.01	0	Inches
50	65	83	102	120	138	157	175	193	211	230	248	266	285	303	321	339	358	376	394	413	431	449	467	486	504	522	540	559	577	595	614	632	0.500
201	228	254	281	308	335	362	388	415	442	469	496	522	549	576	603	630	657	683	710	737	764	791	817	844	871	898	925	951	978	1005	1032	1059	0.450
201	232	263	294	326	357	388	419	450	482	513	544	575	606	638	669	700	731	762	794	825	856	887	918	950	981	1012	1043	1074	1106	1137	1168	1240	0.400
237	269	300	331	363	394	425	456	488	519	550	582	613	644	676	707	738	770	801	832	864	895	926	958	989	1020	1052	1083	1114	1146	1177	1208	1240	0.350
237	268	300	331	362	393	424	456	487	518	549	580	612	643	674	705	736	768	799	830	861	892	924	955	986	1017	1048	1080	1111	1142	1173	1204	1306	0.300
264	297	329	362	395	427	460	492	525	557	590	622	655	687	720	752	785	817	850	883	915	948	980	1013	1045	1078	1110	1143	1175	1208	1240	1273	1306	0.250
264	296	327	358	389	420	452	483	514	545	576	608	639	670	701	732	764	795	826	857	888	920	951	982	1013	1044	1076	1107	1138	1169	1200	1232	1311	0.200
295	327	358	390	422	454	485	517	549	581	612	644	676	707	739	771	803	834	866	898	930	961	993	1025	1057	1088	1120	1152	1184	1215	1247	1279	1311	0.150
295	326	357	388	420	451	482	513	544	576	607	638	669	700	732	763	794	825	856	888	919	950	981	1012	1044	1075	1106	1137	1168	1200	1231	1262	1319	0.100
324	355	386	417	448	479	511	542	573	604	635	667	698	729	760	791	823	854	885	916	947	979	1010	1041	1072	1103	1135	1166	1197	1228	1259	1291	1319	0.050
321	354	373	389	418	456	488	525	572	628	683	711	730	747	777	796	816	831	855	890	902	916	932	1000	1063	1123	1161	1191	1215	1241	1280	1286	1287	0.000

Figure 4.3.3 Gauss Meter Results (Left) & Magnet Testing Area (Right)

This testing allowed the design team to develop a correction factor to convert a magnet manufacturer's reported peak gauss surface value into an average flux value across the length and width

of the generator coils which is a more accurate predictor of the actual flux that the coils are exposed to in operation.

4.3.2 Print Tolerance & Filament

The generator design features a range of complex geometries and low tolerance fits which require a high degree of accuracy to function as designed. Modern 3D printing technology is capable of producing parts of the desired tolerance, but it is a labor-intensive process. To ensure proper fit during assembly, each printer used for printing generator parts was individually tested with prototypes of the various fits utilized in the generator design. The print settings for each prototype fit were gradually adjusted until the desired tolerance was achieved. All the generator's custom parts except for the bearing mounts were constructed out of Polylactic Acid (PLA) filament. 3D printed PLA parts were tensile tested in a universal test machine to determine their material properties and yield stress. These values were subsequently used to confirm that 3D printed PLA could handle the predicted turbine loads for the static parts.

The generator rotors are the only moving part in the assembly. Unlike the rest of the generator parts, the rotors are subject to significant centrifugal loads at turbine operating speeds and therefore required additional stress analysis. The stress simulations for the rotor are shown below in Figure 4.3.4. The magnets were modeled as distributed masses in their respective slots. The image on the left shows the von Mises stress in the rotor for the turbine rotating at 2420rpm which is the rated power speed while the image on the right shows the von Mises stresses in the rotor at a speed of 8500, which is the turbine's speed when subjected to 22m/s of wind speed. The rotor factor of safety was 16.49 and 1.34 at each respective speed.

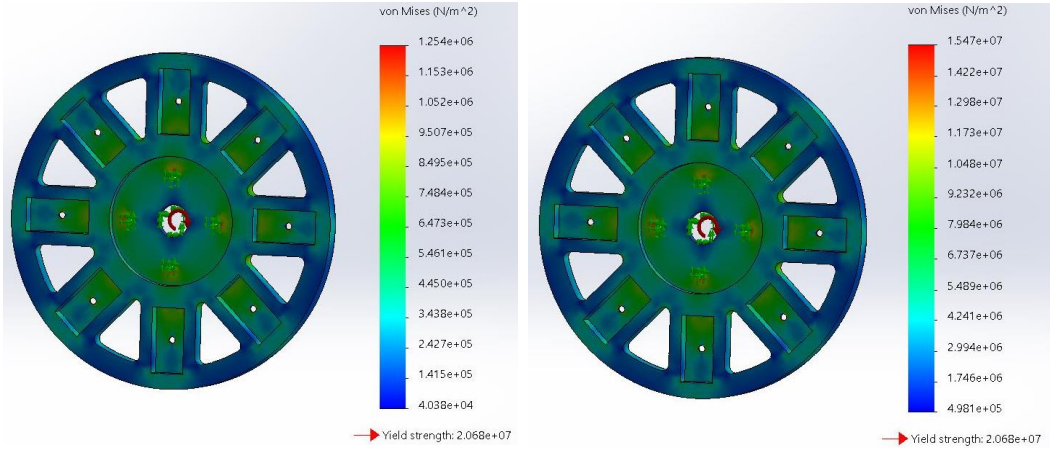

Figure 4.3.4 Rotor Stress Analysis: 2420rpm (Left) & 8500rpm (Right)

4.4 Final Design & Testing

The goal of the final design was not only to develop a generator to compete in the 2021 CWC competition but also to hopefully serve as a modular test platform for future Cal Maritime CWC teams for further refinement and improvements in generator design. The final generator assembly was challenging as the opposite magnet poles generate a significant amount of attractive force between each rotor. In their operating positions with an air gap of 1.95mm, the attractive force between each rotor is approximately 80lbs which means they must be rigidly stabilized throughout the assembly process. Improved methods of locating and stabilizing the rotors

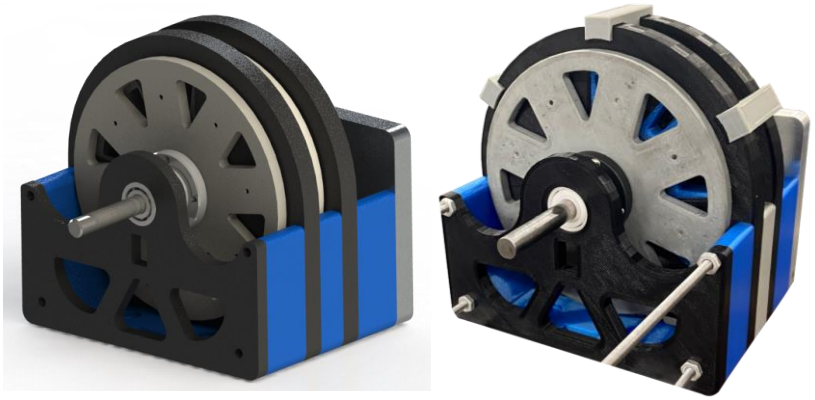

Figure 4.4.1 Final Generator: CAD Model (Left) & Actual (Right)

during assembly have been documented for future teams. The final 2021 generator design is shown in Figure 4.4.1.

Table 4.1.1 displays notable test results obtained while testing the final generator in the wind tunnel at Cal Maritime using the 2021 final blade design.

Average Magnetic Flux Across Coils	1491 Gauss
Voltage Constant (Theoretical)	0.0129 V/RPM
Voltage Constant (Actual)	0.0105 V/RPM
Measured Armature Resistance	1.6 Ω
Generator Cut-in Wind Speed (No Load)	4.1 m/s
Power Generated with Fixed (15 Ω Load)	
8 m/s Wind Speed	15.0 W
9 m/s Wind Speed	23.8 W
10 m/s Wind Speed	33.5 W

Testing results indicated that the generator design was successful. The power output was increased from 2020 and the cut-in wind speed remained materially below the 6.2m/s value from the 2019 teams purchased generator. The additional flux modeling and Gaussmeter testing conduct this year were validated as the 22.8% discrepancy between the theoretical and actual voltage constant were a significant improvement of the 150% error recorded on the 2020 Cal Maritime generator. The remaining discrepancy between the theoretical voltage constant and the experimental voltage constant is likely a result of instrumentation error and magnetic field influences from various pieces of steel hardware used in the final turbine assembly. Additionally, a small amount of radial flux was measured on the rotors which were not theoretically accounted for which may have also contributed to the material difference between the theoretical voltage constant and the experimental voltage constant. Future improvements to this design could include a stepped shaft to eliminate the need to shaft flange collars and the development of aluminum rotors to increase rigidity and further reduce the air gap between the rotors and stators.

Chapter 5: Electronics and Controls

5.1 Overview

The simple electrical system used in this design has two different parts: the turbine-side and the load-side. These two components are connected through the point of common coupling (PCC) and are not connected in any other way. Each side has its own microcontroller for control purposes, which will be discussed later. Figure 5.1.1 displays the general layout of the electrical system.

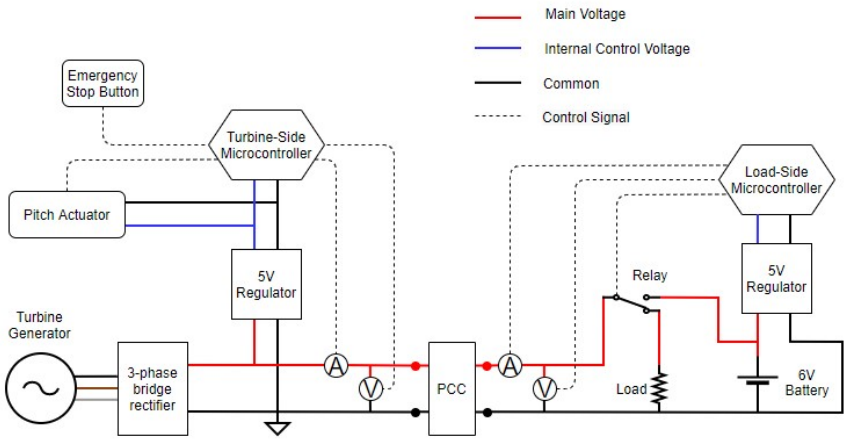

Figure 5.1.1 Electrical System Diagram

The turbine will produce a three-phase AC voltage that will be rectified into DC voltage by using a passive 3-phase bridge rectifier. There are two capacitors wired in parallel, not shown, after the rectifier to smooth out the rectified DC voltage. This decreases the noise in the signal read by the sensors throughout the entire system. The main voltage will split between going to a 5V regulator and the PCC. The 5V regulator powers both the pitch actuator of the variable pitch mechanism and the turbine-side microcontroller. The negative side, seen in the diagram, is a common ground that connects to earth ground on the turbine-side since it must connect to the turbine base plate; this is per the competition rules, as the piece that the turbine mounts to is tied to earth ground to prevent overvoltage of the data acquisition system. The turbine-side microcontroller will read the current, voltage, and emergency stop button status. The only output from this microcontroller is the signal to the actuator.

On the other side of the PCC is the load-side. The main purpose of this side is to switch between the chosen fixed resistive load and a 6V battery by using a single pull double throw (SPDT) relay. The relay sub-circuit uses an NPN transistor circuit that has a flyback diode to prevent a sudden voltage spike that occurs when the current to the relay is changed rapidly. The circuit designed in this system was based on the relay circuit shown in Figure 5.1.2. It is worth pointing out that the 6V battery will constantly power the microcontroller after the voltage is regulated down to 5V. Besides powering the load-side microcontroller, the 6V battery will also be used to power the turbine-side microcontroller when the turbine is in a braking state. In a braking state, the turbine rotor will not be spinning and will therefore not power the turbine-side microcontroller. The 6V battery will allow the turbine side microcontroller to send the signal to the actuator at the right time to pitch the blades back to produce power. The load-side microcontroller will only read the current and voltage. The only output from this microcontroller is the signal for the relay.

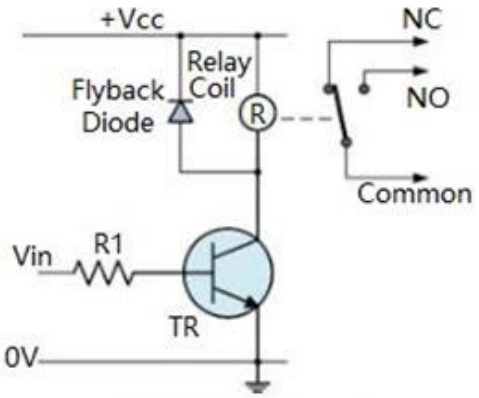

Figure 5.1.2 Relay Circuit [6]

There are other general items that can be discussed when designing this system. Per the rules, the highest voltage that the PCC can receive is 48V. After conducting tests with the generator, the generator would not produce over 48V when using a resistive load that would optimize power production. Therefore, there is no need for regulating the main voltage down before it goes through the PCC. The voltage and current sensors are placed right before and after the PCC so that the control system is controlling towards the values being recording for the competition. These sensors are powered by a 3.3V subsystem from the microcontroller and uses I2C communication to get the read data back to the microcontroller.

To manufacture this electrical system, a printed circuit board (PCB) mill was used and the design was created in EagleCAD. All electrical components were soldered to the board and most connections were made by using traces in the copper on the underside of the board. All other connections were used by either using pin header connections or screw terminals. As for the complete assembly, this entire system was put inside in an enclosed box that utilized cable glands or wall mount connections for any wire coming in or out of the box. In previous years, the electrical system could have been more organized, and it was a smaller goal to have an organized electrical enclosure this year. The final product can be seen in Figure 5.1.3.

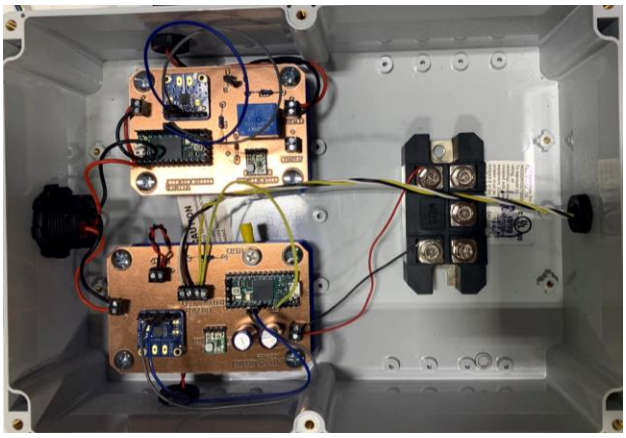

Figure 5.1.3 Final electronics system

5.2 Load Analysis

For the fixed resistance load, the resistance value used was chosen based on how well it optimizes the power production. When changing the resistance value, the current in the system changes therefore changing the power being made. The voltage will not change unless the rotor speed of the generator changes since the generator is a permanent magnet machine. The electrical power is most effective when the power being produced at some rotor speed intersects the peak of the blade's power curve at that associated rotor speed. The downside to having a fixed resistance is that the peaks of each curve cannot intersect for each wind speed curve.

To find an idea for this resistance value, a MATLAB script was written using Qblade and generator data; the data from Qblade was the Cp vs TSR graphs for different wind speeds. The MATLAB code would take this data and determine both the power and rotor speed. The generator data used was the voltage constant of the generator to obtain the voltage coming out of the generator at some rotor speed. Using the generated voltage, the current running through the load is calculated. There will be electrical losses in the system, so the analysis accounts for the armature resistance of the generator. The DC equivalent circuit used for this analysis can be seen in Figure 5.2.1.

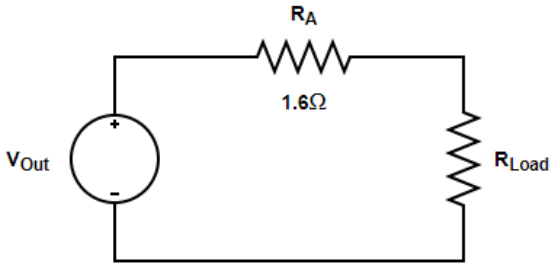

Plotting both the power curve of the generator and the power made from the blades at each wind speed, different resistance values can be used to estimate the optimal resistance value. Figure 5.2.2 shows the results found. The wind speeds used are integer speeds between 5m/s and 11m/s. The objective for finding the optimal resistance is to change the resistance value and see how close it hits the peak of the power curve for each wind speed. The intersection between the airfoil power curves and the load curve gives the theoretical power production that will be made at that wind speed. After narrowing down the resistance value, a theoretical resistance value of 10 ohms was obtained. These calculations were made using theoretical calculations to give an estimated resistance value. The final resistance value used will be narrowed down further through testing of the entire system by using a rheostat.

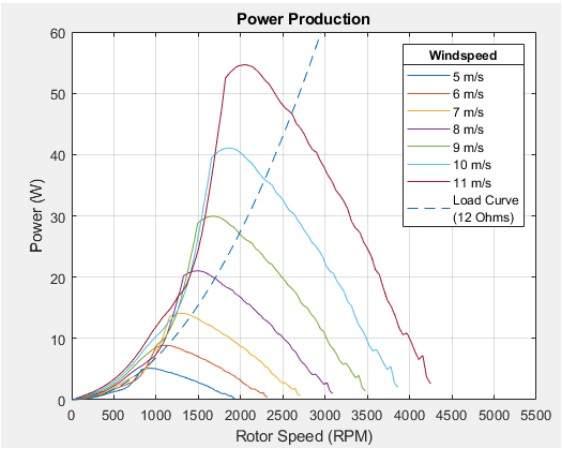

Figure 5.2.2 Load Analysis

5.3 Control

Looking at that previous graph from the load analysis, the power being made at 11m/s is considered the rated power. After 11m/s wind, the power output needs to be the same as what was made at 11m/s. The method used to regulate power in this design is by using the variable pitch mechanism to change the angle of attack of the blades. Since the generator is a permanent magnet machine, the voltage to rotor speed has a linear relationship. If the rotor speed decreases, the voltage will decrease and therefore will cause the power to decrease. The amount of angle needed to execute is where the main control comes into play. For this, another MATLAB analysis was created using the results from the previous load analysis. The same power curve for the output power of the generator was used and the horizontal line is the rated power from the load analysis. What needs to be found is the angle of pitch that intersects the same point as the rated power line and electrical power curve. To do this, Cp vs TSR diagrams for different angles of attack were created using Qblade. The power curve was calculated the same way as in the previous analysis, but here the wind speed is the independent variable. This analysis was run at different wind speeds to get an idea of what the pitch needs to be set to make produce rated power. As an example, the analysis was

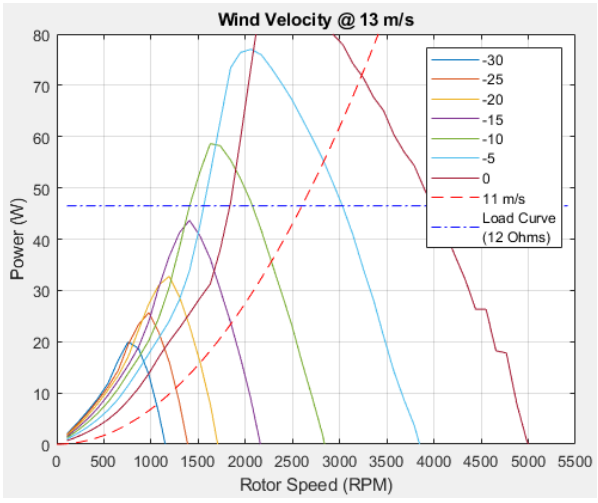

Figure 5.3.1 Pitch Analysis

conducted at an input wind speed of 13m/s and the resulting plot can be seen in Figure 5.3.1. The approximate angle of attack needed is -7.5°. The table below, Table 5.3.1 shows the estimated angles of attack needed for the corresponding input wind speeds along with the necessary stroke of the actuator needed to obtain this angle. The values in the chart were calculated by analyzing the geometry of the variable pitch mechanism. These values for the pitch and stroke command will be confirmed or changed when doing final testing.

Wind Speed (m/s)	Estimated Pitch (degree)	Actuator Stroke (mm)	Actuator Stroke Percent (%)
11	0	32.5	65
12	-5	30.5	61
13	-7	29.8	60
14	-9	29.1	58
15	-11	28.4	57
16	-12.5	27.9	56
17	-14	27.4	55
18	-16	26.7	53

Table 5.3.1 Relationship between actuator stroke and angle of pitch

This analysis also helps with getting a starting point of what the control variables need to be since the controlling will be done by using a PID control. The variable pitch is controlling towards the rated power which is the power being produced at a wind speed of 11m/s. The power being produced will be calculated using the current and voltage sensor. The data read by the sensor is averaged over a series of values to get a better idea of the actual power. The error is calculated by taking the power being produced and subtracting it by the rated power. The calculated error is used to calculate the control signal needed via a PID control scheme. Once the control signal is calculated, the signal is then commanded by the microcontroller to the actuator. Being a closed feedback loop, the error is calculated by using the new produced power, and the process repeats.

To limit the control from going past the optimal pitch angle, a simple if-statement is used to max the control signal out the signal needed for the optimal pitch angle. With the variable pitch mechanism, there are liming positions that change the operation of the mechanism and therefore have another check for that within this control loop. The control loop can be seen in Figure 5.3.2. The signal to control the actuator uses a PWM signal where a 1.0-millisecond pulse duration commands the actuator to fully retract, and a 2.0-millisecond pulse duration commands the actuator to fully extend. The function used to output the signal to the actuator uses a desired stroke percentage (1-99%) as an input. This percentage is then used to calculate the appropriate millisecond pulse command.

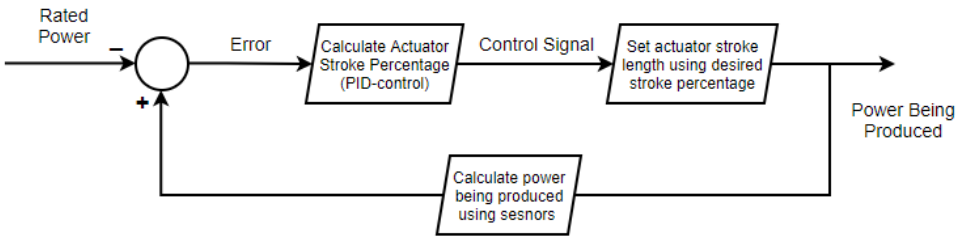

Figure 5.3.2 Pitch Control Loop

The other controls used in this system include switching between the battery and the load during start-up. For start-up, the blades would start at a non-optimal pitch to cut in much earlier than with an optimal pitch. This allowed for a very low cut-in speed. Once the wind speed was past 4.5m/s the battery would then connect therefore turning on the turbine-side microcontroller since the non-optimal pitch would not produce enough power to turn the microcontroller on. Once the microcontroller is powered, the first command is to set the actuator stroke to the optimal angle of pitch. When this command occurs, the turbine produces enough power to then keep the microcontroller running. This is when the battery disconnects. With the values that control this transition, the initial switch off and then back to the resistive load occurs between 4.5m/s and 5m/s where no points are being deducted off our total score for producing negative power.

5.4 Safety

To satisfy the safety aspect of the durability task, the turbine needs to reduce its power to less than 10% of the rated power. The power is reduced the same way when regulating the power output; the variable pitch feathers the blades. To get down to such low power, the blade angle is changed so dramatically that it will not produce any lift and therefore stop the rotation of the driveshaft to the

generator. The act of feathering this far is considered braking (State 3). Braking needs to occur when either the emergency stop button is pressed or when the load is disconnected. These actions will only be done at wind speeds higher than 6.5m/s. Some of the conditions in the control logic limit when the battery connects to the whole system. One of the main goals for this year was to have a low cut-in wind speed and one way to help lower that is by starting up with the electronics not being powered. For an overview of the entire safety control system, a state diagram can be seen below in Figure 5.4.1 and Figure 5.4.2 to understand the conditions better.

To sense the state of the emergency stop button (a normally closed button), 3.3V is run through the button and back to the ground through a resistor. A digital pin on the turbine-side microcontroller is used to sense if there is 3.3V (HIGH) or 0V (LOW) before the resistor. If this pin reads a HIGH signal, then the button is not pressed, and normal operation can continue. If this pin reads a LOW signal, then the button is pressed, and feathering the blades is the next action to occur. Per the rules, a low amperage signal needs to be used. This is completed by using a resistor with a large amount of resistance (2kΩ) to ensure the current stays low. The load-side microcontroller will sense when the emergency stop button is pressed by looking at the voltage and currents being read by the sensor since this microcontroller is on the other side of the PCC than the emergency stop button. Once the current is less than 0.1A, then the battery will connect. To prevent the battery from connecting at the start with no wind speed, there is a buffer state that will wait until the produced current is over 0.15A and the voltage is less than 5.5V to then start sensing the current. These values were chosen through testing our final design.

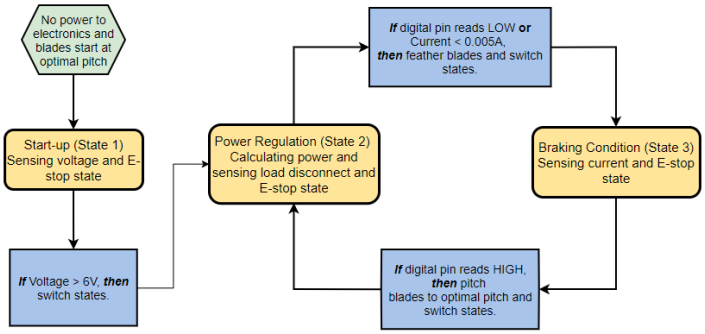

Figure 5.4.1 Turbine-Side State Diagram

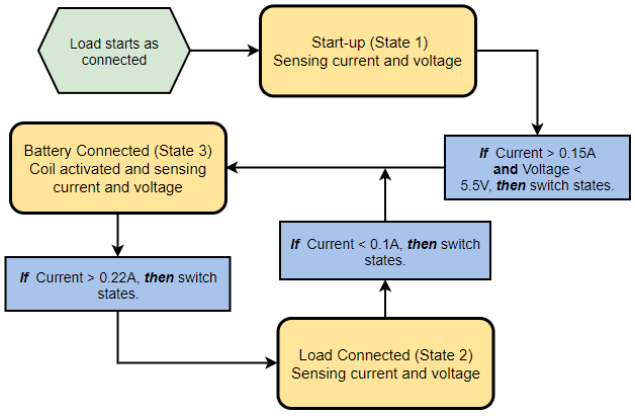

Figure 5.4.2 Load-Side State Diagram

To sense the load disconnect, the two current sensors will be used. When the load is disconnected at the PCC, the circuit becomes an open circuit. Knowing this, the current will read theoretically 0A. A threshold current variable is used so that the value of this can be changed to account for what the sensor reads when there is no current flowing. Both the turbine-side microcontroller and load-side microcontroller will sense this immediately and will therefore feather the blades and connect the battery. When the load is reconnected, the only criteria that must be met to pitch the blades back is the emergency stop button is not pressed. The turbine-side microcontroller only needs to sense this state because it can only do that when it is powered and therefore implies that the load is connected. Once the microcontroller knows that the criteria have been met, the actuator will start at the optimal pitch to go back into power production (state 2). To reconnect the load, the only criteria that need to be met is that the current running through the system needs to be positive. A positive current in this situation means the potentials being created by the turbine are greater than that of the battery.

Chapter 6: Final Design

6.1 Turbine Stress

The turbine is capable of surviving all expected operating conditions. However, if placed in a situation of 22m/s winds and no control then both the blades and variable pitch mechanism will fail. If these situations do become necessary, the blades could be strengthened by using alternative materials and

the variable pitch design could include a larger connection screw between the blade mount and shaft. However, in the wind industry it is important to lower cost to stay competitive with natural gas, thus designing and increasing cost for a situation that is extremely unlikely to occur (losing control and load at 22m/s) is not of utmost importance. Not to say safety is not a concern, but there is a necessary compromise to determine if the increase in cost is less than the risk of this possible situation.

Condition	Wind Speed (m/s)	Rotor Speed (RPM)	Pitch (Degrees)	Blades FS	Generator FS	Variable Pitch FS
Operating (No Pitch)	11	2420	0	10.4	16.49	1.24
Max Operating (Pitch)	18	2420	17.5	10.4	16.49	1.24
Extreme (Parked)	22	0	90	3.85	∞	∞
Extreme (Survival)	22	8500	0	0.8	1.337	0.15

Table 6.1.1: Turbine Factor of Safety

6.2 Results

The turbine has been completed and fully assembled in the wind tunnel has been conducted on Thursday, May 13th. The test conducted included all parts of the test that would be seen during an actual competition. For the cut-in wind speed test, the turbine started producing positive power at 3m/s and up until 4.5m/s. For the power-curve test, the results at each integer wind speed can be seen in Table 6.2.1. For the power regulation test, the control system did pitch the blades to decrease the power output and did control the rotational speed very well. The problem with this test was that the control system did not allow for consistent power output to be very smooth. The cause for this unsteady regulation of power is most likely due to the resolution of the actuator chosen or how clean the command signal is being given by the microcontroller. To fix this, the problem would need to be narrowed down and then analyzed. If the actuator resolution is the problem, then a new actuator needs to be chosen. If the signal is not clean enough, then an electrical solution needs to be found. For the durability test, the yaw system worked as intended resulting in never losing power production. For the safety task, the emergency stop button was pressed at a wind speed of 13m/s and worked as intended to reduce the rotor speed to almost a standstill. The load disconnect did not work as intended. There was an assumption that when the load was pulled, the actuator could feather the blades before the microcontroller lost power. This did not happen and the blades did not feather enough to reduce power to within 10% of the rated power. The solution to this is either to find a fast actuator which would most likely result in the same outcome and would make power regulation harder. The other solution is to short the phases of the generator. This could have been easily added into the control system if there was more time. For an actual competition, this would have been resolved before coming to the actual competition. Throughout the year there were a few issues that the team ran into, but in the end, were able to produce an incredible final product (Figure 6.2.2) and the turbine is expected to perform extremely well in final testing.

Power		
U (m/s)	Weighting	P (W)
5	0.7	1.2
6	0.8	4
7	0.8	8.5
8	0.7	15
9	0.4	22
10	0.3	30.9
11	0.1	38

Table 6.2.1: Power Curve Test Results

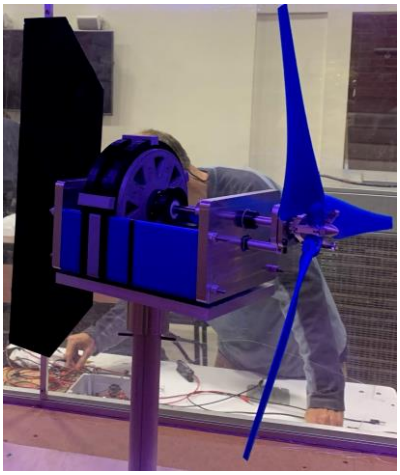

Table 6.2.2: Final Turbine Assembly

Bibliography

[1] Brown,T., Eagle, F., Kruschke, S., Jo, C., Nguyen, A., Skarin,J., Smith, M.,Sprague, T., Rodriguez, S., Wang, J., Vargas, A., (2020). Technical Design Report (CWC Submission). California State University, Maritime Academy, Vallejo, CA. Retrieved from https://www.energy.gov/eere/collegiatewindcompetition/

[2] Bear, N., Graham, A., Ito, D., Kizilkaya, D., Logier, R., Rodriguez, S., Sadamune, A. (2019). Technical Design Report (CWC Submission). California State University, Maritime Academy, Vallejo, CA. Retrieved from https://www.energy.gov/eere/collegiatewindcompetition/

[3] Hooper, Gillian (2020). Material/Mechanical Lab Report.California State University, Maritime Academy, Vallejo, CA.

[4] Manwell, J. F., McGowan, J. G., & Rogers, A. L. (2009). Wind Energy Explained: Theory, Design and Application. Chichester, U.K: Wiley.

[5] Airfoiltools.com. (2020). RUTAN WING AIRFOIL (Amsoil2-Il).

[6] Apogeeweb. (2020). What Is A Flyback Diode or Freewheeling Diode and It's Applications. Apogeeweb. Retrieved from https://www.apogeeweb.net/electron/flyback-diode-flywheel-diode-applications.html

[7] Moreels, D., & Leijnen, P. (2019, September 30). *This Inside-Out Motor for EVs Is Power Dense and Finally Practical*. IEEE Spectrum: Technology, Engineering, and Science News. Retrieved from https://spectrum.ieee.org/transportation/alternative-transportation/this-insideout-motor-for-evs-is-power-dense-and-finally-practical

[8] K&J Magnetic Inc. (n.d.). *K&J Magnetics - Magnetic Field Visualization*. kjmagnets.com. https://www.kjmagnetics.com/magfield.asp?pName=BX082-N52.

[9] Fizzics. (n.d.). *Define-Tesla.png*. Magnetic Flux Density. https://www.fizzics.org/magnetic-flux-density-notes-and-video/ .

[10] Latoufis, K.c., et al. Axial Flux Permanent Magnet Generator Design for Low Cost Manufacturing of Small Wind Turbines. *Wind Engineering*, vol. 36, no. 4, 2012, pp. 411–431., doi:10.1260/0309-524x.36.4.411.

[11] Niessen, F., & Malte. (2013). *Winding Scheme Calculator*. Homebuilt Electric Motors. https://www.bavaria-direct.co.za/scheme/calculator/.

[12] MITOPENCOURSWARE. 2006. Area And Bending Inertia Of Airfoil Sections. [online] Available at: .

[13] Young, W. C., Budynas, R. G., Roark's Formulas for Stress and Strain, 7th edition, 2002, McGraw Hill